Spin-torch experiment on reaction centers of Rhodobacter sphaeroides

Sai Sankar Gupta, K.B.

Chapter 3

Dynamic asymmetry in the Special Pair of *Rhodobacter sphaeroides* observed by photochemically induced dynamic nuclear polarization ^{13}C NMR

Abstract

Electron transfer in photosynthetic reaction centers (RCs) of the photosynthetic purple bacteria *Rhodobacter (R.) sphaeroides* wild type (WT) occurs almost exclusively via the A branch. The primary electron donor, the Special Pair (P), is constituted by two bacteriochlorophyll *a* (BChl) cofactors. Here we investigate the internal dynamics of P by ^{13}C photochemically induced dynamic nuclear polarization (photo-CIDNP) solid-state magic-angle spinning (MAS) NMR dipolar correlation spectroscopy and site-selective ^{13}C isotope enrichment of P in the ground state. Solid-state photo-CIDNP excitation leads to strong signal enhancement in two-dimensional dipolar-assisted rotational resonance (DARR) MAS NMR experiments. 2D spectra collected with different mixing times allow for both the assignment of signals and mapping of rapid oscillatory motion of P around its ground state equilibrium structure with atomic selectivity from the kinetics of the ^{13}C spin-diffusion processes. With a rate matrix analysis the dynamic partial averaging of dipolar interactions is resolved for individual ^{13}C spin pairs. The data provide convincing evidence that the collective modes are localized towards the P_M bacteriochlorophyll that is connected to the active branch accessory bacteriochlorophyll via His M202 and a water molecule and possible implications of the localized dynamics for symmetry breaking and charge transfer are discussed.

3.1 Introduction

In photosynthetic reaction centers (RCs) of the purple bacterium *Rhodobacter (R.) sphaeroides* WT (for reviews, see (Hoff & Deisenhofer, 1997; Hunter *et al.*, 2008)), the primary electron donor is a bacteriochlorophyll *a* (BChl) dimer, called the Special Pair P, comprising two dimer halves P_L and P_M (Figure 3.1A). Two additional BChl cofactors called accessory BChls (B_A & B_B), two bacteriopheophytins (Φ_A & Φ_B), two quinones and a non-heme iron are organized into two pseudo-symmetric branches named A and B (Figure 3.1B). It was found that collective nuclear motion on the potential energy surface of the excited state of the primary electron donor P* enables the charge transfer in the RC which is initiated by $P_L^+P_M^-$ internal charge transfer character, followed by the formation of $P^+B_A^-$ and $P^+\Phi_A^-$ intermediates over the active A branch (Moore *et al.*, 1999; Yakovlev *et al.*, 2010a). Excitations that enter the RC from the antenna are thought to lose excitonic character and gain polaronic character by coupling to two specific collective nuclear modes, a higher frequency intradimer mode of around 130 cm^{-1} and a low frequency protein mode of ~30 cm^{-1} (Novoderezhkin *et al.*, 2004). This

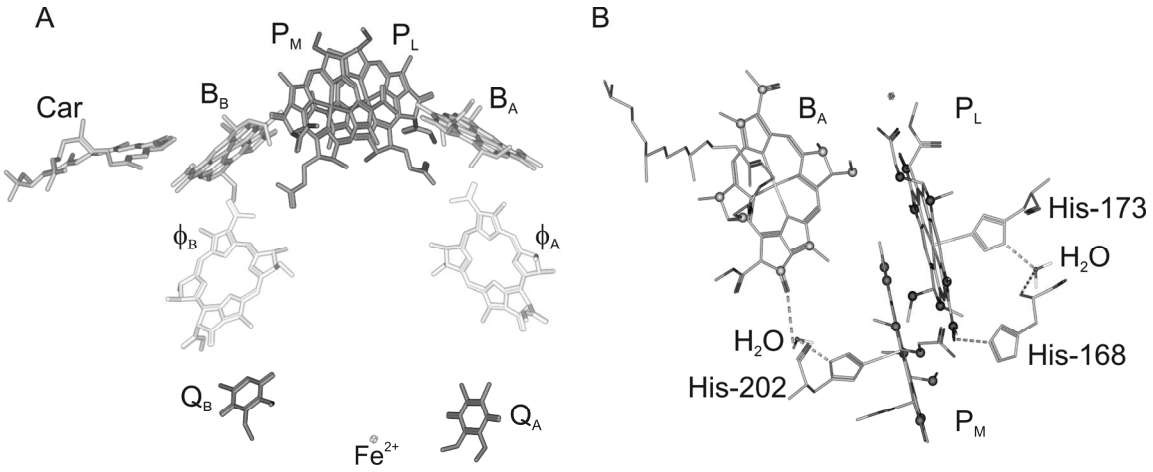

Figure 3.1 (A) The arrangement of cofactors in reaction centers (RCs) of *Rhodobacter (R.) sphaeroides* wild type (WT). The primary electron donor, the special pair, is formed by the two bacteriochlorophyll *a* (BChl) molecules P_L and P_M. B_A and B_B are accessory BChl cofactors. Φ_A and Φ_B are bacteriopheophytin (BPhe) cofactors. The two ubiquinone-10 cofactors Q_A and Q_B are localized on the acceptor side with a non-heme iron in between. Side chains are omitted to provide a clear view on the active parts. The apparent symmetry of the cofactor arrangement is broken by a carotenoid cofactor (Car). The light-induced electron transfer occurs selectively via branch A. (B) Another view of spatial arrangement of the cofactors P_L (top, right, isotope labels in blue), P_M (bottom, middle, isotope labels in red) forming the Special Pair and an accessory bacteriochlorophyll on the A branch (B_A) along with hydrogen bondings with nearest water molecules. [PDB entry 1M3X, the figure has been made with Accelrys Discovery Studio].

low frequency mode has been proposed to be connected to a protic species, *e.g.* the reorganization of the phenolic OH of Tyr M210 between P and B_A or the water molecule that is hydrogen bonded to the B_A ring V keto functionality and the N_π of the HisM202 that is axially coordinated with the N_τ to the Mg^{2+} of the P_M. Such hydrogen bondings can stabilize a $P^+B_A^-$ charge transfer contribution in a collinear proton coupled electron transfer (PCET)-type process from the P* to the B_A along the chain of polar groups Mg(P_M)–N–C–N(HisM202)–HOH(55)–O=(B_A) (Moore *et al.*, 1999; Yakovlev *et al.*, 2002; Potter *et al.*, 2005; Grondelle & Novoderezhkin, 2006; Alia *et al.*, 2009; Yakovlev *et al.*, 2010b; Wawrzyniak, 2011).

Stark effect measurements on RCs of *R. sphaeroides* that are sensitive to changes in the electronic charge distribution following excitation reveal a large change in dipole moment, 8.6 D, and the excited state of the Special Pair contains significant $P_L^+P_M^-$ charge-transfer character (Deleeuv *et al.*, 1982; Lockhart & Boxer, 1987, 1988). These observations are consistent with hole-burning experiments (Johnson *et al.*, 1991; Purchase & Völker, 2009), where large values for the total Huang-Rhys factor of ~1.5 and the Special Pair marker mode of ~120 cm^{-1} have been reported and attributed to a geometry change in the excited state induced by the primary charge separation (Reddy *et al.*, 1992; Lyle *et al.*, 1993).

As demonstrated also by differences in vibrational frequencies (Palaniappan *et al.*, 1993), the structure of the two cofactor halves (Camara-Artigas *et al.*, 2002a) and their chemical shifts (see chapter 2), the symmetry between the two cofactors is already broken in the ground state (Schulten *et al.*, 2002; Daviso *et al.*, 2009c). In addition, theoretical calculations indicate that the axial histidines donate electron density to P_L and P_M and that the orientation of the 3^1 acetyl group in P_L and protein surrounding modulate the distribution of the excess electron density over the two halves of the special pair (Alia *et al.*, 2004; Wawrzyniak *et al.*, 2011). For the radical cation state, it has been shown by ^1H ENDOR (Lendzian *et al.*, 1993) that the electron-spin density is asymmetrically distributed in favor of P_L in the Special Pair. Recent ^{13}C and ^{15}N laser-flash photo-CIDNP MAS NMR (Daviso *et al.*, 2009b; Daviso *et al.*, 2010) allowed to determine the electronic

structure of the HOMO at atomic resolution. In this study it has also been shown that there is excess spin density on the P_L in the radical cation state. Hence the asymmetry of the HOMO is an intrinsic property of the Special Pair complex with its axial histidines and is caused by small differences between the thermally averaged geometries of the two cofactors in their surrounding protein matrix. Here we explore a new avenue by probing the dynamics of the BChl in the Special Pair by labelling of the macrocycle rings at various positions (Figure 3.1B). These positions were ^{13}C labelled by culturing *R. sphaeroides* in a medium containing a selectively isotope labelled precursor of the tetrapyrrole synthesis, 3-$^{13}C_1$-δ-aminolevulinic acid (3-ALA) (Figure 3.2).

The solid-state photo-CIDNP effect (for reviews, (Jeschke & Matysik, 2003; Daviso *et al.*, 2008b; Matysik *et al.*, 2009)) has been observed for the first time in 1994 by Zysmilich and McDermott (Zysmilich & McDermott, 1994) in RCs of *R. sphaeroides* and allows enhancement of ^{13}C signals of the Special Pair by a factor of more than 10,000 (Prakash *et al.*, 2005; Prakash *et al.*, 2006). Upon illumination, a highly electron spin-ordered radical pair is formed, and nuclear polarization is established in nearby nuclei by up to three mechanisms, called three-spin mixing (Jeschke, 1997, 1998), differential decay (Polenova & McDermott, 1999) and differential relaxation (Goldstein & Boxer, 1987; McDermott *et al.*, 1998). The combined operation of these mechanisms in generating photo-CIDNP is now well understood (for a review, see (Daviso *et al.*, 2009a)). In the meanwhile, the effect has also been observed in RCs of plants, of green sulfur bacteria and of purple non-sulfur bacteria (Matysik *et al.*, 2009). The signal enhancement provided by the solid-state photo-CIDNP effect may thus be considered an intrinsic property of natural photosynthetic RCs and allows directly resolving the signals of ^{13}C atoms within the RC (Matysik *et al.*, 2009). In chapter 2 an experimental scheme is introduced for two-dimensional chemical-shift correlation spectroscopy using dipolar-assisted rotational resonance (DARR) following excitation by photo-CIDNP (Takegoshi *et al.*, 2001). In the DARR experiment, nuclear polarization transfer is driven by a spin-diffusion-type mechanism while the heteronuclear (^1H-

^{13}C) dipolar couplings are re-established by continuous ^{1}H rf irradiation on a rotary resonance condition $\omega_1 = n\omega_r$, with ω_1 the nutation frequency of the ^{1}H rf irradiation, ω_r the spinning frequency, and n= 1 or 2 (Levitt *et al.*, 1988; Oas *et al.*, 1988). Such an irradiation leads not only to a broadening of the ^{13}C lines but also to an active recoupling at second-order resonance conditions which is based on the matching of the nutation frequency of the I spins to the isotropic chemical-shift difference of S-spin pairs ($\omega_1 = n\omega_r \pm \Delta\ \omega_{iso}$) (Scholz *et al.*, 2008). DARR spectra can provide ^{13}C assignments and provide information about the local mobility. The decay rates of the diagonal peaks are related to local mobility, and the build-up of the cross peaks depends on the magnitude of the dipolar couplings, which are maximum if the molecule is rigid.

In an analogy to other dipolar processes, such as the Förster transfer of optical excitations (Förster, 1948), spin diffusion in static samples can be described phenomenologically by a rate constant W_{ij} that characterizes transfer of magnetization between two nuclei *i* and *j* and is given by (Abragam, 1961)

$$W_{ij} = \frac{1}{2}\pi * g_o^{ij}(0) * \omega_{ij}^2, \qquad (3.1)$$

with the dipolar coupling constant ω_{ij} between the two spins being given by

$$\omega_D^{ij} = -2\left(\frac{\mu_0}{4\pi}\right)\left(\frac{\hbar\gamma_i\gamma_j}{r_{ij}^3}\right). \qquad (3.2)$$

The function $g_0^{ij}(0)$ describes the intensity of the normalized zero-quantum line at frequency zero, which can be approximated by the overlap between the two NMR single-quantum lines of spins *i* and *j*, assuming that the broadening mechanisms are uncorrelated. Since the dipolar coupling constant between the two spins depends on the inverse third power of the distance r, spin diffusion is a short- to intermediate-range effect with $W_{ij} \propto r_{ij}^{-6}$. Using this distance dependence, solid-state NMR experiments based on spin diffusion have been introduced to obtain distance information in solids (Douglass & McBrierty, 1978; McBrierty, 1979; Caravatti *et al.*, 1982; Szeverenyi *et al.*, 1982; Henrichs & Linder, 1984; Caravatti *et*

al., 1985) in analogy to the nuclear Overhauser effects in liquids (Hull & Sykes, 1975; Kalk & Berendsen, 1976; Gordon & Wüthrich, 1978; Kumar *et al.*, 1980; Kumar *et al.*, 1981).

Although dipolar couplings are in zeroth-order approximation averaged by MAS (Andrew *et al.*, 1959; Lowe, 1959), spin diffusion has also been observed in polycrystalline solids under MAS (Kubo & McDowell, 1988), opening the possibility to use distance restraints derived from spin-diffusion data as a tool for protein structure determination (Griffiths *et al.*, 2000; Mulder *et al.*, 2000; van Rossum *et al.*, 2000; Castellani *et al.*, 2002; de Boer *et al.*, 2002; Hiller *et al.*, 2005; van Gammeren *et al.*, 2005; De Paepe *et al.*, 2008; Gardiennet *et al.*, 2008; Loquet *et al.*, 2008). With MAS, spin diffusion is promoted not directly by the dipolar-coupling Hamiltonian. It involves higher-order terms in the average Hamiltonian expansion that have a form similar to the static dipolar Hamiltonian (Grommek *et al.*, 2006). Since the spin-diffusion rate constant is proportional to the square of the effective dipolar-coupling strength, dynamic processes will lead to a slowdown of the spin-diffusion process due to the reduction in the strength of the dipolar couplings.

3.2 Materials and Methods

3.2.1 Sample preparation

The selective isotope labelling in RCs of *R. sphaeroides* is achieved by feeding the bacteria with selectively labelled 3-$^{13}C_1$-δ-aminolevulinic acid (3-ALA), which is a

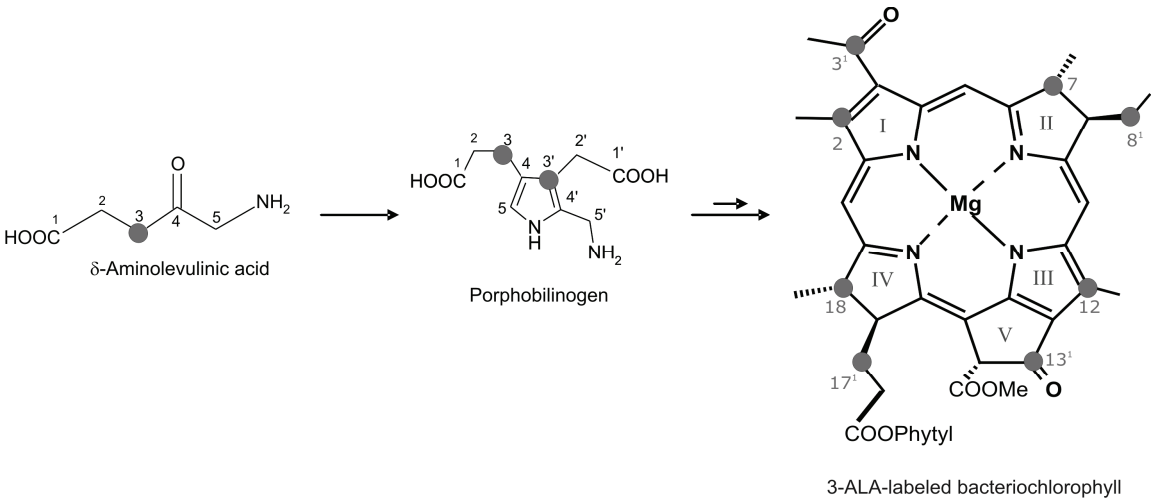

Figure 3.2 Biosynthetic pathway for the formation of selectively ^{13}C isotope labelled bacteriochlorophyll a (BChl) by feeding the bacteria with 3-^{13}C-δ-aminolevulinic acid (3-ALA).

precursor for the formation of BChl and BPhe, and leads to a ^{13}C enrichment of ~60%. The 3-ALA (Figure 3.2) has been purchased from Buchem B.V. (Apeldoorn, The Netherlands). The RCs were isolated as described earlier (Shochat *et al.*, 1994) and the quinones were removed by incubating the RCs at a concentration of 0.6 µM in 4% LDAO, 10 mM o-phenanthroline, 10 mM Tris buffer, pH 8.0, containing 0.025% LDAO and 1 mM EDTA (Okamura *et al.*, 1975). Approximately 15 mg of RC protein complex embedded in LDAO micelles were used for a NMR experiment.

3.2.2 MAS NMR experiments

NMR experiments were performed with an Avance DMX-200 (4.7 Tesla) NMR spectrometer equipped with a 4 mm MAS probe (Bruker BioSpin GmbH, Karlsruhe, Germany). The sample was loaded into a clear 4 mm sapphire rotor and inserted into the MAS probe. It was frozen slowly at a low spinning frequency of 600 Hz to ensure a homogeneous sample distribution against the rotor wall (Fischer *et al.*, 1992).

All two-dimensional (2D) ^{13}C-^{13}C photo-CIDNP DARR MAS NMR experiments were recorded with a MAS frequency of 8 kHz and at a set temperature of 223 K using continuous illumination with white light (Matysik *et al.*, 2000b). The spectra were measured in 64 scans with 200 t_1 increments and a recycle delay of 4 s, resulting in a total experiment time of 11 h for a mixing time of 2 s. Spin-diffusion mixing times between 0.02 to 10 s were used. The FID was detected with proton decoupling using the TPPM sequence (Bennett *et al.*, 1995). The optimum length of the ($\pi/2$) carbon pulse, determined on uniformly ^{13}C labelled tyrosine, was ~4.0 µs, corresponding with the nutation frequency of 62.5 kHz. All ^{13}C-MAS NMR spectra were referenced to the carbonyl resonance of solid tyrosine•(HCl) set to 172.1 ppm.

2D spectra were processed using the TopSpin (version 2.1) software package (Bruker BioSpin GmbH, Rheinstetten, Germany). A sine-squared window function was applied along with zero filling to 1024 data points in both

dimensions. All 2D data sets were deconvoluted using the mixed line shape function with a 90% Gaussian and 10% Lorentzian contribution to obtain integrated intensities.

3.2.3 The rate-matrix approach

To obtain quantitative data for the spin-diffusion rate constants of Eq. (3.1), a rate-matrix approach has been applied. The diagonal peaks were normalized with the sum of the respective cross peak intensities. These integrated and normalized diagonal and cross-peak intensities were used to determine the spin-diffusion rate constants using Matlab scripts (Matlab, The MathWorks, Natick, Massachusetts, USA). The time evolution of the spin-diffusion process is described by the differential equation

$$\frac{d}{dt}\vec{p}(t) = W\vec{p}(t), \qquad (3.3)$$

where $\vec{p}(t)$ is the time-dependent vector of all the polarizations of the involved resonances and the matrix W contains the rate constants W_{ij} in the off-diagonal elements while the diagonal elements are given by (Ernst & Meier, 1998)

$$W_{jj} = -\sum_{i \neq j} W_{ij} - R_1^{(j)}. \qquad (3.4)$$

Here, $R_1^{(j)}$ is the longitudinal relaxation rate constant of the resonance *j*. A sparse rate matrix with non-zero elements for all ^{13}C spin pairs that are separated by a distance less than 6 Å was used. Non-linear least-square fitting was used to optimize the spin-diffusion rate constants and the relaxation-rate constants in order to obtain information about the possible polarization-transfer pathways. For the fit, a series of 2D photo-CIDNP DARR MAS NMR spectra with spin-diffusion mixing times from 0.02 s to 10 s (not shown) were used. Figure 3.3, showing a spectrum with a mixing time of 2 s, is an example of this series of spectra. The obtained rate constants are shown in Table 3.2 & Table 3.3 and plots of some of the experimental cross-peak and diagonal-peak intensities together with the best fitted curves are shown in Figure 3.4 and Figure 3.5. The intensity of the diagonal peak at zero mixing time has been normalized to unity.

3.3 Results & discussion

3.3.1 Signal assignment

Many ^{13}C resonances of the BChl cofactors of the Special Pair have already been assigned in previous studies on unlabelled (Prakash *et al.*, 2006; Daviso *et al.*, 2009b), and selectively with 4-ALA (Schulten *et al.*, 2002; Daviso *et al.*, 2009a) and 5-ALA (Prakash *et al.*, 2007) labelled WT RCs. While the 4-ALA and 5-ALA label patterns allow the study of the aromatic carbons of the BChl and BPhe macrocycles, 3-ALA labelling leads to isotope enrichment of the more peripheral carbon positions (Figure 3.1A and 3.2). This labelling pattern is particularly suitable for observation of spin diffusion because it provides a broad range of distances as well as chemical-shift differences between pairs of labels. Figure 3.3 shows a 2D photo-CIDNP DARR MAS NMR spectrum of a selectively labelled 3-ALA (WT) RC sample.

In this experiment, the spin-diffusion mixing time was set to 2 s to observe as many cross peaks as possible. In Chapter 2, similar experiment had been performed but with a mixing time of 1 s. The corresponding 1D spectra shown on the top and on the side demonstrates that all signals are emissive (negative). The negative sign of the signal has been explained by the dominance of the three-spin mixing mechanism which involves a symmetry breaking process by the nuclear Zeeman, hyperfine and anisotropic interactions. This leads to emissive signals, independent of the sign of all other interactions involved.

Only ^{13}C nuclei from the two BChl cofactors of the Special Pair and the primary electron acceptor BPhe of the A branch that form the primary radical pair are observed with photo-CIDNP MAS NMR on RCs of *R. sphaeroides* WT (Prakash *et al.*, 2005; Prakash *et al.*, 2006; Daviso *et al.*, 2009a; Daviso *et al.*, 2010). The earlier studies have demonstrated that P_L carries a higher electron spin density and shows generally higher signal intensities than P_M. Further, the two-dimensional spectrum displayed in Figure 3.3, we observe two correlation networks; and they have been assigned in the similar way *i.e.*, the one with the higher signal intensities is from P_L and labelled in blue, while the second one is assigned to P_M

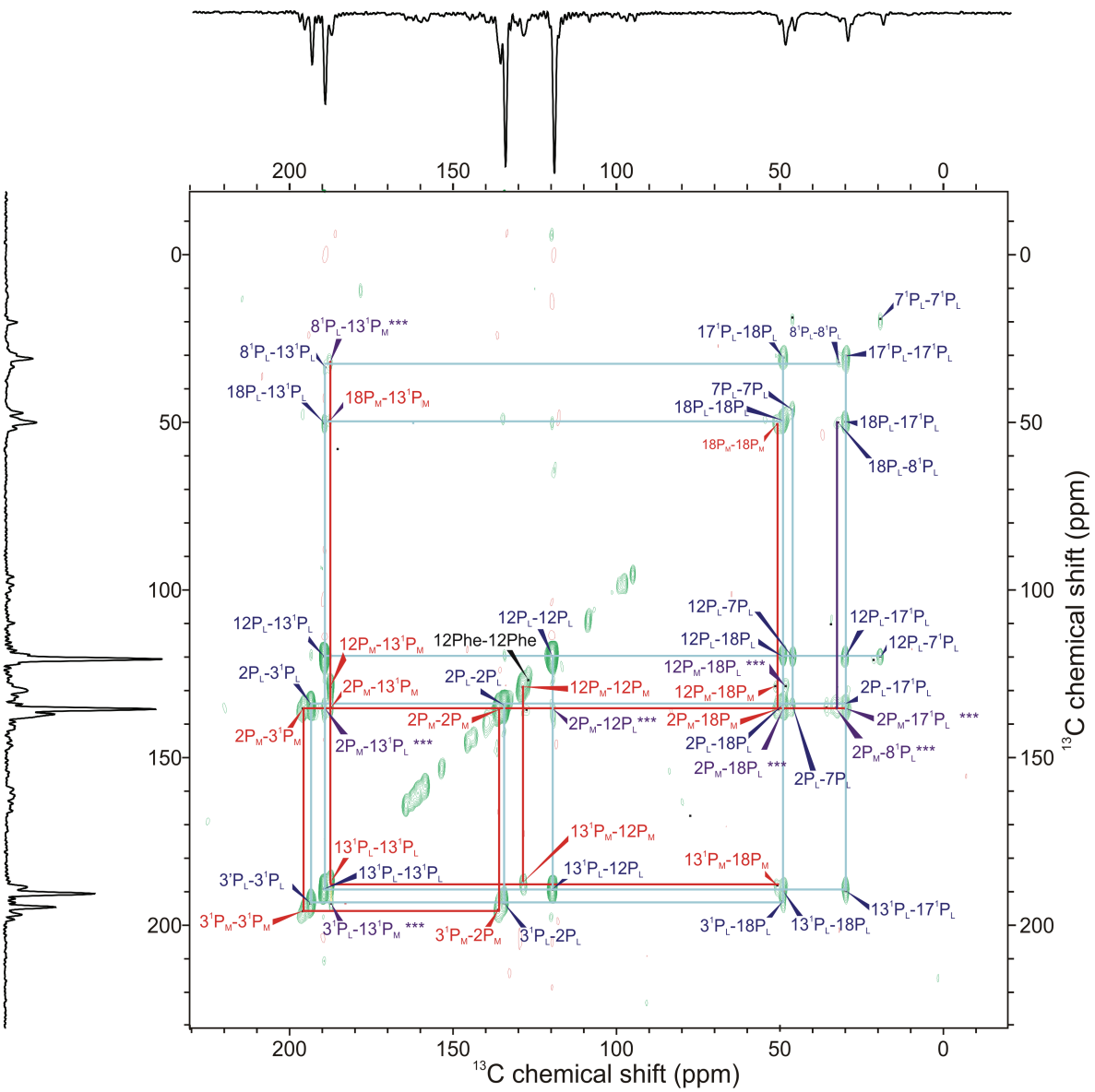

Figure 3.3 Two-dimensional photo-CIDNP DARR MAS NMR spectra of 3-ALA labelled RCs of *R. sphaeroides* WT obtained at a temperature of 223 K with a spin-diffusion mixing time of 2 s and a MAS frequency of 8 kHz. Two correlation networks are distinguished: One network is assigned to P_L (blue) while the other is assigned to P_M (red). Intermolecular cross peaks are shown in purple.

and is labelled red. The isolated C7/C8 pair can be conveniently added into the red network. In addition, at 126.9 ppm (C12 Phe), a signal occurs without any correlation, and is therefore assigned to the primary acceptor.

The strategy applied for assigning the spectrum in chapter 2 as been applied here. Starting point for the assignments can be the C3^{1} resonances, which appear in the carboxylic region at lowest field, *i.e.*, at 195.6 ppm for the red and at

Table 3.1 Assignment of the signals from 3-ALA-labelled from Special Pair in BRCs obtained with continuous illumination.

^{13}C position	P_L (ppm)	P_M (ppm)
2	134.3	136.0
3'	193.5	195.6
7	46.1	48.3
8'	32.1	-
12	119.5	128.8
13'	189.4	187.5
17'	29.9	28.4
18	49.1	50.9

193.5 ppm for the blue network. Alternatively, the signals of the two aromatic carbon positions, C2 and C12, provide a starting point, since these carbons obtain the strongest enhancement by the TSM photo-CIDNP effect (Prakash *et al.*, 2005). Aliphatic carbons C7 and C18, located on the macrocycle, resonate with a chemical shift around 50 ppm. Two labelled side chain carbons, $C8^1$ and $C17^1$, resonate around 30 ppm. Table 3.1 summarizes the assignments. Since the photo-CIDNP polarization transfer among the labelled ^{13}C atoms is mediated by spin diffusion, which operates through space providing access to the intermolecular distances and thus acting as a "Spin-torch" experiment. In addition to the two intramolecular networks, there are few cross-peaks, labelled purple, that arise from correlations between P_L and P_M. Examples of such correlations between P_L and P_M are $C3^1(P_L)$ / $C13^1(P_M)$ (7.1 Å), $C8^1(P_L)$ / $C13^1(P_M)$ (7.1 Å) and from P_M to P_L: $C12(P_M)$ / $C18(P_L)$ (13.1 Å), $C2(P_M)$ / $C18(P_L)$ (5.5 Å), $C2(P_M)$ / $C8^1(P_L)$ (7.9 Å), $C2(P_M)$ / $C17^1(P_L)$ (6.3 Å), $C2(P_M)$ / $C12(P_L)$ (8.4 Å), $C2(P_M)$/ $C13^1(P_L)$ (8.8 Å).

3.3.2 Spin Diffusion Measurements

The spin-diffusion rate depends directly on the strength of the dipolar couplings. Local dynamics will lead to partial averaging of dipolar couplings and, therefore, also to a reduction of the spin-diffusion rate constants compared to the corresponding rigid spin configuration The rate constants extracted from the DARR spectra are shown in Table 3.2 and Table 3.3, while some characteristic experimental sets for the build up and decay of cross-peak and diagonal-peak intensities, together with the analysis from the nonlinear least squares fitting of the rate matrix in eq (3.4), are shown in Figure 3.4 and Figure 3.5. The intensity of the diagonal peak at zero mixing time has been normalized to unity.

Due to the sparse labelling pattern of the BChl rings (Figure 3.1 and 3.2), the shorter internuclear distances are optimal for direct transfer of polarization within pairs of labels. The distances for intramolecular pairs are equal in P_L and P_M: $C17^1/C18$ (2.5 Å), $C7^1/C8^1$ (2.5 Å), $C2/C3^1$ (2.8 Å), and $C12/C13^1$ (2.8 Å). In addition, for the overlap region of P_L and P_M, the intramolecular distances for the $C2/C3^1$ pairs (2.8 Å) are significantly shorter than the shortest intermolecular distance between pairs of labels in the ring and in the side chain positions, C2 (P_L)/$C2^1$ (P_M) (3.8 Å). Polarization transfer between the nearby ^{13}C nuclei is mainly direct and can provide information about the local mobility.

The DARR spectra (Figure 3.3) also reveal correlation peaks for long range transfer up to 13 Å. Examples of long distance correlations between P_L and P_M are $C8^1(P_L)$ / $C13^1(P_M)$ (7.1 Å), $C2(P_M)$ / $C8^1(P_L)$ (7.9 Å), $C2(P_M)$ / $C12(P_L)$ (8.4 Å) and $C12(P_M)$ / $C18(P_L)$ (13.1 Å). Very little direct polarization transfer over such a long distance is possible and these cross peaks are attributed to relayed multi-step polarization transfer. The quantitative analysis of the spin-diffusion pathways with the relaxation matrix confirms that these long distance correlation events are mediated by relayed transfer involving various nuclei in the network of labels. Figure 3.6 shows four examples of such networks of multi-step transfers. In Figure 3.6A, the correlation network linking $C2(P_M)$ and $C8^1(P_L)$, over a distance of 7.9 Å,

Table 3.2 ^{13}C-^{13}C correlation pairs (diagonal peaks) with calculated rate constants for decay of the peaks obtained by nonlinear least squares fitting of the relaxation matrix.

No	Correlation pair	Calculated rate constant (sec^{-1})	Displayed
1	$C2(P_M)$	0.07	A
2	$C3^1(P_M)$	0.84	B
3	$C12(P_M)$	0.35	C
4	$C13^1(P_M)$	0.00	D
5	$C18(P_M)$	0.09	-
6	$C2(P_L)$	0.31	A
7	$C3^1(P_L)$	0.12	B
8	$C7(P_L)$	0.81	-
9	$C8^1(P_L)$	0.02	-
10	$C12(P_L)$	0.37	C
11	$C13^1(P_L)$	0.21	D
12	$C17^1(P_L)$	0.00	I
13	$C18(P_L)$	0.23	J

Table 3.3 ^{13}C-^{13}C correlation pairs (cross peaks) with distances and calculated rate constants for the rise of the peaks obtained by nonlinear least squares fitting of the relaxation matrix.

No	Correlation pair	Distance (Å)	Calculated rate constant (sec^{-1})	Displayed
1	$C2(P_M)$ / $C\text{-}3^1(P_M)$	2.8	3.02	E,F
2	$C2(P_M)$ / $C18(P_M)$	5.1	0.18	-
3	$C2(P_M)$ / $C2(P_L)$	3.8	0.00	-
4	$C2(P_M)$ / $C3^1(P_L)$	5.1	0.00	-
5	$C2(P_M)$ / $C18(P_L)$	5.5	0.08	-
6	$C3^1(P_M)$ / $C2(P_L)$	4.9	0.22	-
7	$C3^1(P_M)$ / $C3^1(P_L)$	6.0	0.00	-
8	$C3^1(P_M)$ / $C7(P_L)$	5.4	0.33	-
9	$C3^1(P_M)$ / $C8^1(P_L)$	5.6	1.93	-
10	$C3^1(P_M)$ / $C12(P_L)$	5.9	0.35	-
11	$C3^1(P_M)$ / $C17^1(P_L)$	5.8	0.00	-
12	$C3^1(P_M)$ / $C18(P_L)$	5.6	0.19	-
13	$C12(P_M)$ / $C13^1(P_M)$	2.8	0.61	G,H
14	$C12(P_M)$ / $C3^1(P_L)$	6.0	0.08	-
15	$C13^1(P_M)$ / $C18(P_M)$	6.0	0.14	-
16	$C18(P_M)$ / $C2(P_L)$	5.9	0.04	-
17	$C2(P_L)$ / $C\text{-}3^1(P_L)$	2.8	1.61	E,F
18	$C2(P_L)$ / $C18(P_L)$	5.0	0.41	-
19	$C3^1(P_L)$ / $C7(P_L)$	5.6	0.15	-
20	$C7(P_L)$ / $C8^1(P_L)$	2.5	0.00	-
21	$C8^1(P_L)$ / $C12(P_L)$	5.2	0.00	-
22	$C12(P_L)$ / $C13^1(P_L)$	2.9	2.19	G,H
23	$C13^1(P_L)$ / $C17^1(P_L)$	4.9	0.51	-
24	$C17^1(P_L)$ / $C18(P_L)$	2.5	10.00	K,L

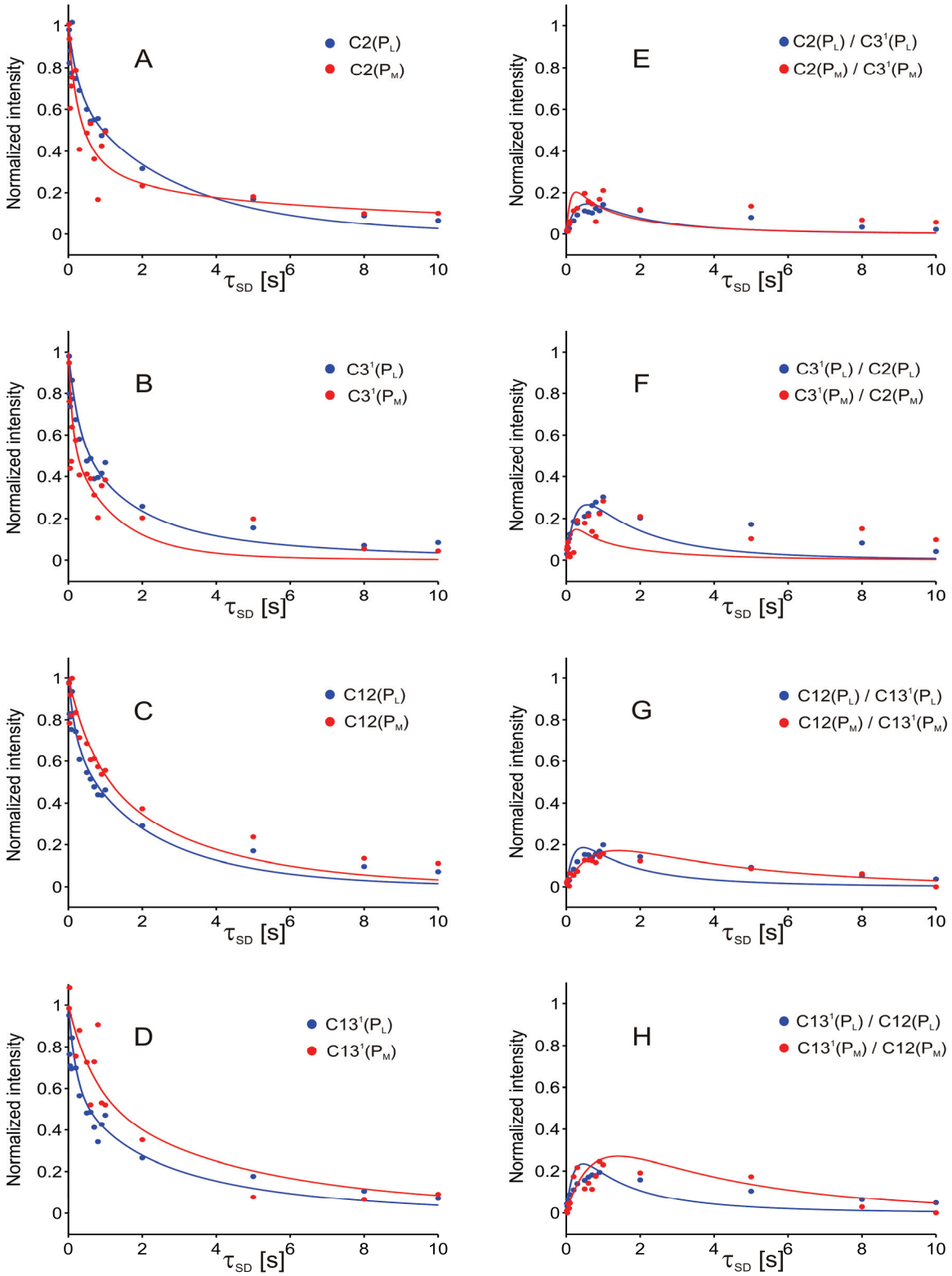

Figure 3.4 Decay of normalized diagonal peaks of P_L (blue) and P_M (red) and evolution of corresponding cross peaks of P_L (blue) and P_M (red) for selected ^{13}C-^{13}C correlation pairs.

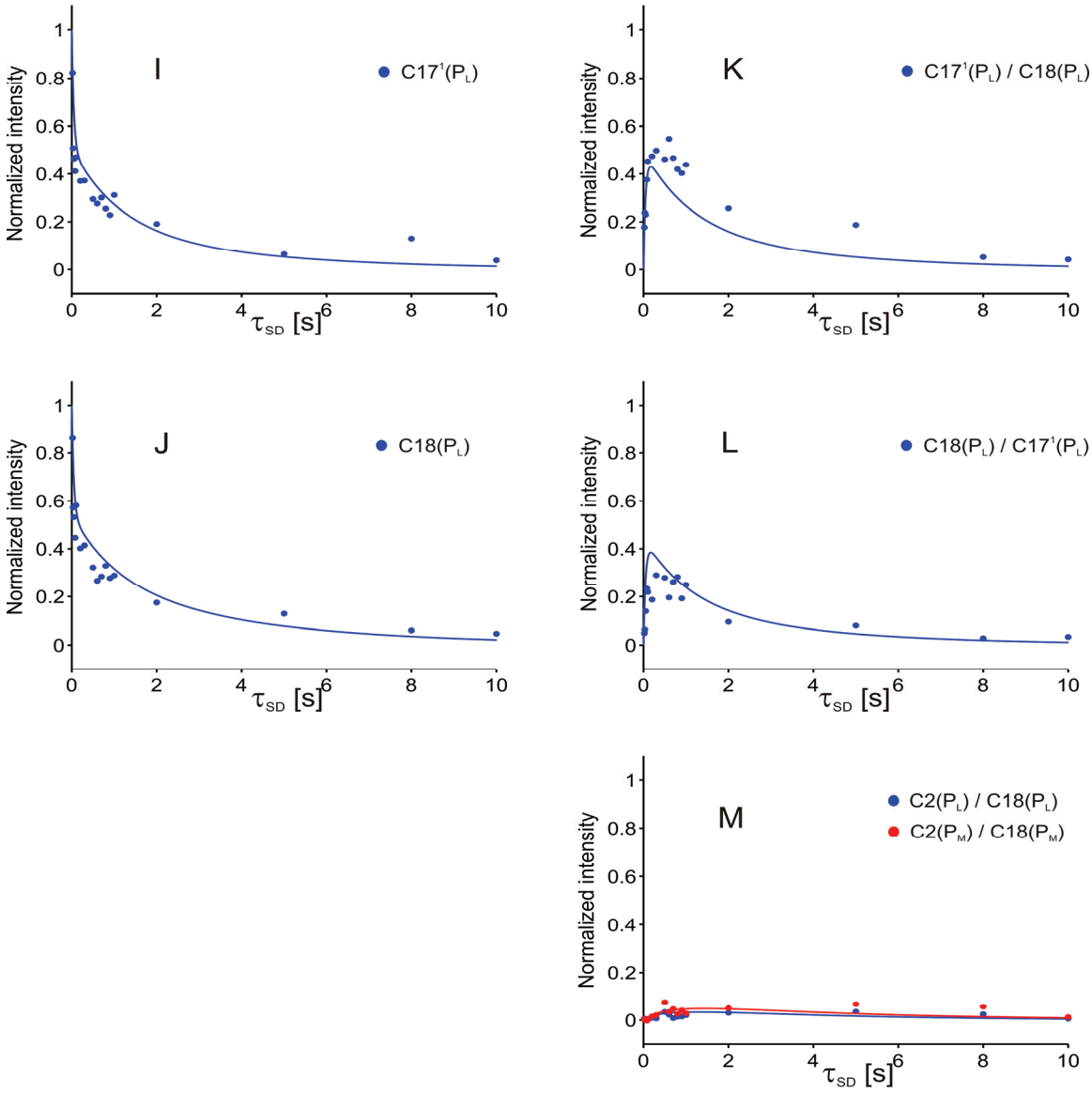

Figure 3.5 Decay of normalized diagonal peaks of P_L (blue) and P_M (red) and evolution of corresponding cross peaks of P_L (blue) and P_M (red) for selected ^{13}C-^{13}C correlation pairs.

is presented. The transfer occurs via two steps: first from C2(P_M) to C3^1(P_M) (2.8 Å), and then to C8^1(P_L) (5.6 Å). In Figure 3.6B, the most efficient pathway allowing for the correlation between C2(P_M) and C12(P_L), at a distance of 8.4 Å, is indicated. The transfer occurs via five steps, first from C2(P_M) to C2(P_L) (3.8 Å), then via C18(P_L) (5.0 Å), to C17^1(P_L) (2.5 Å), C13^1(P_L) (4.9 Å) and finally to C12(P_L) (2.9 Å). In this pathway, the C2(P_M) and C2(P_L) act as a bridge to transfer the polarization between the two cofactors of the Special Pair.

In Figure 3.6C, the transfer over a distance of 13.1 Å between C12(P_M) to C18(P_L) can proceed by several pathways. From the analysis of rate constants, we see that the polarization is transferred to C12(P_M) via C13^1(P_M) (2.8 Å), C18(P_M) (6.0 Å), C2(P_M) (5.1 Å), C3^1(P_M) (2.8 Å) and finally to C18(P_L) (5.6 Å). In Figure 3.6D, another example of long-distance transfer is presented. While the distance between C8^1(P_L) to C13^1(P_M) is 13.1 Å, the polarization is transferred via C3^1(P_M) (5.6 Å), C2(P_M) (2.8 Å), C18(P_M) (5.1 Å) and finally to C13^1(P_M) (6.0 Å). In any case, the occurrence of such long-distance contacts demonstrates that reduction of dipolar couplings by motional averaging is limited, and confirms that packing effects on the BChl comprising the Special Pair from the protein surrounding lead to a ground state potential energy surface that enhances the mobility of the rings for selective collective modes. A single, well defined and narrow NMR signal

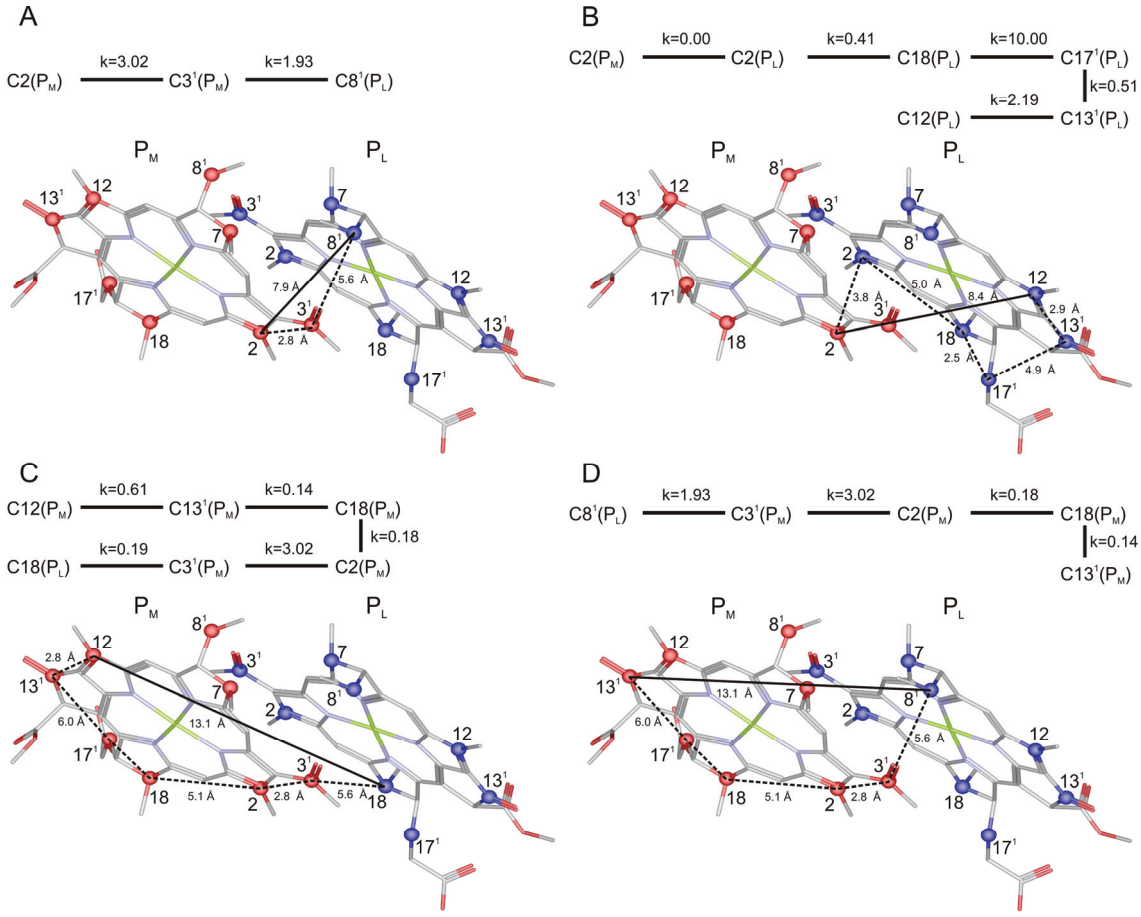

Figure 3.6 Selected polarization-transfer pathways obtained from the rate-matrix analysis. The solid line indicates the shortest distance between two carbons, while the dashed lines show the possible relay transfer between those two carbon atoms.

component is observed for every ^{13}C label of P by partial dynamic averaging of the supermolecular structure, instead of *e.g.* spectral doubling or gross inhomogeneous broadening due to polymorphism (Schulten *et al.*, 2002; Prakash *et al.*, 2005). This contrasts with optical spectroscopy that operates on a much shorter time scale and reveals quasi-static site disorder, variations of the structure of the special pair in the protein complex. In the optical experiments variations of the site energies lead to inhomogeneous broadening of the optical absorption profile (Hunter *et al.*, 2008).

The left part of Figure 3.4 (Plots A-D) compares the signal decay on selected carbons of both halves of the Special Pair. Those selected carbon atoms displayed there, show a different kinetics trend depending on their positions in the Special Pair. The difference is summarized in Figure 3.7, Table 3.2 and Table 3.3. The origin of this difference, however, is not clear. It may be due to enhanced mobility in low frequency collective vibrational modes that gives spectral density at the higher end of the T_1 NMR sensitivity region to drive spin-lattice relaxation. Alternatively, less dynamics can lead to an increase of the spin diffusion efficiency and more rapid decay. Hence, although plots A-D of Figure 3.4 clearly demonstrate that the symmetry in the Special Pair regarding the dynamics is broken, it is difficult to conclude for which of the two rings there is more constrained dynamics.

To determine which of the two sides is more flexible, the time dependence of the build up of the cross peaks is studied. This can be correlated with the spin diffusion efficiency, while T_1 relaxation of the carbons is not relevant on that short time scale. The kinetics of the decay of the diagonal-peaks is shown in the left parts of Figure 3.4 and 3.5. These two figures are summarized in Figure 3.7A and Table 3.2. Here the magnitude is visualized by the radius and color of the circle that matches the labelled position on Special Pair. The circles on the right side are larger than for the left hand side of the pseudo–C_2 axis. The kinetics of the build-up of the cross-peaks is shown in the right parts of Figure 3.4, 3.5 and is summarized in Figure 3.7B and Table 3.3**.** In this Figure 3.7B, the magnitude of the

spin-diffusion rate constants is visualized by the line width of an ellipse connecting the two ^{13}C labels involved. The spin diffusion in the right half of the Special Pair supermolecule is faster than the spin diffusion in the left half. Interestingly, this difference cannot be attributed to the two individual cofactors P_L and P_M, and is associated with the left and right half of the Special Pair supermolecule. All three pairs on the right half (C2/C18 and C12/C13^1 of P_L as well as C2/C3^1 of P_M) are significantly stronger coupled than the two pairs on the left half (C2/C18 and C12/C13^1 of P_M as well as C2/C3^1 of P_L). In addition the pair (C12/C13^1 of P_M) at the edge of the inactive branch appears to be rather mobile.

3.3.3 Possible implications for directed electron transfer

The Special Pair supermolecule is thus relatively rigid towards the P_L side, while the P_M side shows significantly more mobility that partially averages the dipolar couplings and leads to longer buildup times than for the corresponding pairs on the A side (Figure 3.7B). This shows that there is dynamic asymmetry in the Special Pair. The NMR detects a constrained but homogeneous structure with rapid averaging of dynamic disorder revealed by narrow lines in the spectra. In contrast, optical spectroscopy suggests heterogeneity which is revealed by inhomogeneous line broadening due to site disorder of the system (Reddy *et al.*, 1992; Reddy *et al.*, 1993). In addition, there is converging evidence for asymmetry of the average electronic structure, both for the ground- and the excited state, from distortions imposed upon the structure by geometric constraints and steric hindrance of the side chains. The protein environment also affects the electronic structure of the porphyrin ring via the electron-phonon coupling (Chapter.2; Lendzian *et al.*, 1993; Yamasaki *et al.*, 2008; Daviso *et al.*, 2009c).

To add to the structural basis for the asymmetry of the dynamics in the ground state observed with NMR, an analysis of polymorphism of the P_L and P_M in the available X-ray structures with resolution better than 3Å is shown in Figure 3.8, using the Normal-Coordinate Structural Decomposition (NSD) method (Jentzen *et al.*, 1997). A vibrating molecule moves along its normal coordinates,

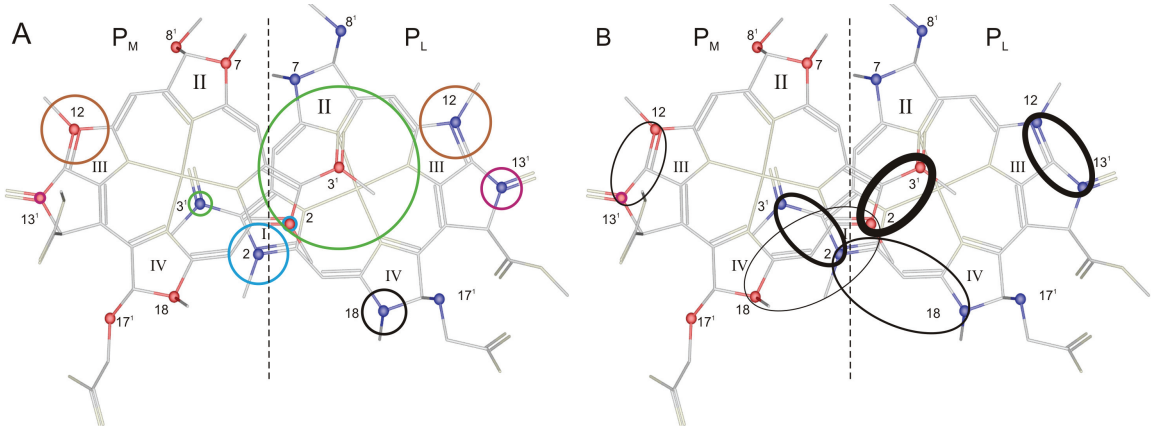

Figure 3.7 Spin-diffusion dynamics in the Special Pair. (A) The rate constants of carbon atoms from their diagonal peaks (The magnitude is visualized by the radius). (B) The rate constants of carbon atoms from their cross peaks (The magnitude of spin-diffusion-rate constants are visualized by the linewidth of an ellipse connecting the two ^{13}C labels).

and the molecular distortion is expressed as a sum of displacements along 3N-6 normal coordinates. For porphyrin systems, the macrocycle deformations are soft modes of distortion and correspond with the six lowest-frequency normal modes of the molecule. This method quantifies the nonplanarity of porphyrin structures by displacements along the lowest-frequency normal coordinates of the macrocycle (Jentzen *et al.*, 1998; Shelnutt *et al.*, 1998).

The bar graph of the displacements along the low frequency ring modes in Figure 3.8, indicates similarities and differences for the P_L and P_M in 3 different crystal structures. The largest variability is found for both BChls along the saddling and ruffling normal coordinates, which represent the softest modes of distortion and corresponds with the lowest frequency vibrations, usually around 65 cm^{-1} and 88 cm^{-1} in porphyrins (Shelnutt *et al.*, 1998). In P_L, the displacement along the doming mode coordinate is remarkably persistent and is ~ 1.1 Å in the three structures (Figure 3.8A). The doming mode has a characteristic frequency around 135 cm^{-1} in porphyrins (Shelnutt *et al.*, 1998). In contrast, the displacement for doming in P_M is small (Figure 3.8B). This makes it easier to deform the P_M ring than the P_L ring, in line with the NMR data that show enhanced dynamics for the P_M relative to the P_L. In addition, for the NSD analysis in Figure 3.8 the magnitude of the displacements along the saddling and ruffling coordinates for the P_M

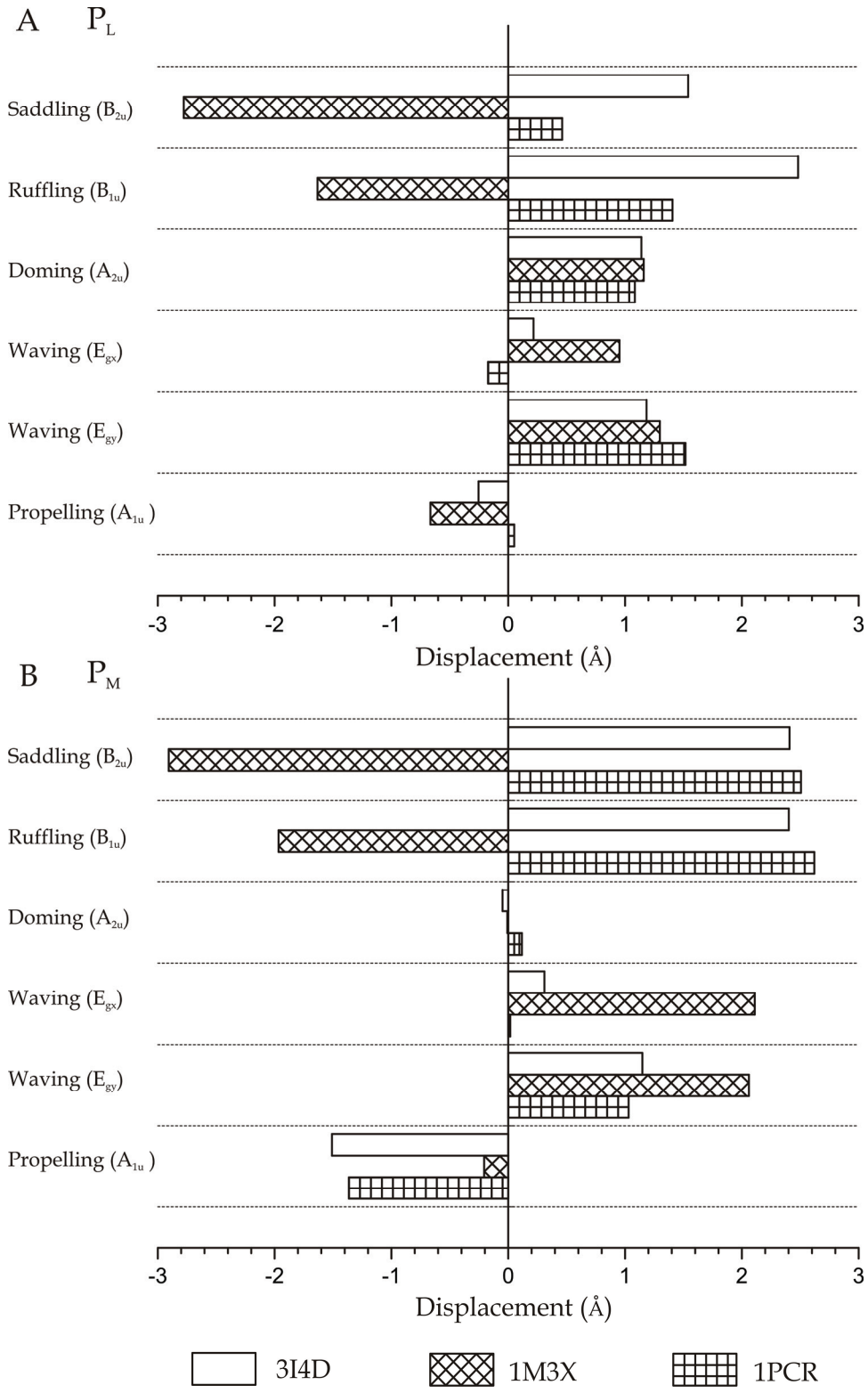

Figure 3.8 Nonplanarity of the P_L (A) and P_M (B) for three different X-Ray structures of *R. sphaeroides* RCs along the six lowest frequencies normal coordinates of the macrocycles.

appears larger than for the P_L. In this way the static structural variation in the X-ray data matches the dynamics observed in NMR data.

In early theoretical treatments of electron transfer in proteins, a coupling of the system to many thermal vibrational modes is invoked to obtain a rapid transfer process (Marcus, 1956b, 1965; Marcus & Sutin, 1985). In contrast with the Marcus treatment, in recent Redfield matrix analyses the charge separation dynamics is determined by the combined displacement along two selective vibrational modes to produce a high forward transfer rate and a low probability for back transfer. A 130 cm^{-1} collective mode connected with the intermolecular dynamics within the special pair governs the displacement along the first reaction coordinate (Novoderezhkin *et al.*, 2004). A planar ring structure is anomalous for a five-coordinated Mg^{2+}. NMR and modeling studies have provided evidence that the ground state exhibits HisL173$^{\delta+}$–$P_L^{\delta-}P_M^{\varepsilon-}$-HisM202$^{\delta+}$-$H_2O^{\delta-}$ charge transfer character (Schulten *et al.*, 2002; Prakash *et al.*, 2007; Alia *et al.*, 2009; Daviso *et al.*, 2009b; Wawrzyniak *et al.*, 2011; Wawrzyniak, 2011). In this scheme, the HisM202 is stabilizing both P_M and the attached water molecule by hydrogen bonding and partial charge transfer at both imidazole nitrogens (Alia *et al.*, 2009). In addition, EPR shows that after the release of an electron into the active branch the P_M carries excess positive charge. In contrast, the studies on RCs of *R. sphaeroides* by Stark spectroscopy indicate that the excited state of the Special Pair contains charge-transfer character of the form $P_L^+P_M^-$ (Lockhart & Boxer, 1987, 1988). In parallel hole-burning experiments showing a marker mode of ~120 cm^{-1}, indicate a persistent change upon excitation (Reddy *et al.*, 1992; Lyle *et al.*, 1993).

Our analysis suggests that the special pair dynamics involved in the initiation of charge transfer is asymmetric and restricted to the overlap region formed by the rings I of the P_L and the P_M, where most of the dynamics is in the P_M. According to the NMR and X-ray, the P_M is in an anomalous planar average structure with enhanced mobility in selective modes. The release of free energy in the excited state could then activate its deformation for mediating charge transfer by a geometry change, possibly towards a more domed conformation of the P_M and involving lowering of the free energy by the damping of vibrations. Finally, the dynamics detected with the NMR affects the ring structure and should give

rise to fluctuations in the $P_L^{\delta-}P_M^{\varepsilon-}$ charge transfer character. Indeed, in analyses of X-ray structures, charge density distributions depend on the polymorphism in the structure (Wawrzyniak *et al.*, 2011).